

Extension of the modified Bai-Wierzbicki model for predicting ductile fracture under complex loading conditions

B. Wu  | X. Li | Y. Di | V. Brinnel | J. Lian | S. Münstermann

Integrity of Materials and Structures, Steel Institute, RWTH Aachen University, Intzestrasse 1, D-52072 Aachen, Germany

Correspondence

Dr B. Wu, Integrity of Materials and Structures, Steel Institute, RWTH Aachen University, Intzestrasse 1, D-52072 Aachen, Germany.

Email: bo.wu@iehk.rwth-aachen.de

Funding information

German Research Foundation (Deutsche Forschungsgemeinschaft), Grant/Award Number: BL 402/33-1, KL 500/82-1

Abstract

The ductile fracture behaviour of metallic materials is strongly dependent on the material's stress state and loading history. This paper presents a concept of damage initiation and failure indicators and corresponding evolution laws to enhance the modified Bai-Wierzbicki model for predicting ductile damage under complex loading conditions. The proposed model considers the influence of stress triaxiality and the Lode angle parameter on both damage initiation and the subsequent damage propagation. The model parameters are calibrated for C45E + N steel using a series of mechanical tests and numerical simulations. The enhanced approach is applied to the modelling of various mechanical tests under proportional and non-proportional loading conditions and successfully predicts the ductile damage behaviour in these tests.

KEYWORDS

damage mechanics model, ductile fracture, non-proportional loading, stress state

1 | INTRODUCTION

In metallic materials, ductile fracture occurs after significant plastic deformation. Dimple fracture and shear fracture are the dominant ductile fracture mechanisms.¹ Various damage mechanics models have been proposed for predicting ductile failure. Three main groups of models are available: micromechanically motivated porous plasticity models,²⁻⁹ continuum damage mechanics (CDM) models¹⁰⁻¹² founded on thermodynamic considerations, and macroscopic,

phenomenological strain-based failure models, which consider a stress-state-dependent strain to failure.^{13,14} The stress state can be characterised by stress triaxiality and the Lode angle parameter. The classical models typically consider the influence of stress triaxiality on damage evolution, and increased attention has been given to the Lode angle parameter over the last few years.^{8,9,14-16} Among the recently proposed Lode-dependent models, the phenomenological Bai-Wierzbicki (BW) model¹⁶ formulates the stress triaxiality and Lode angle parameter in both the plasticity description

Statement: All of the other co-authors have approved of this submission.

Nomenclature: A_u , Uniform elongation; c_{θ}^{ax} , c_{θ}^d , c_{θ}^s , c_{θ}^e , m , Parameters for plasticity description of the Bai-Wierzbicki model; C_1 – C_4 , Parameters of the damage initiation locus; C_5 – C_8 , Parameters of the D_{cr} locus; D , Damage variable; D_{cr} , Critical damage variable to fracture; D_i , Damage initiation indicator; D_f , Failure indicator; D_0 , External diameter of the ring specimen; d_0 , Internal diameter of the ring specimen; G_f , Energy dissipation parameter; h , Height of the ring specimen; h_0 , Original height of the ring specimen; k , Shear flow stress; q, p, r , Stress invariants; R_{eH} , Upper yield point; R_{eL} , Lower yield point; R_m , Tensile strength; $\bar{\epsilon}^p$, Equivalent plastic strain; $\bar{\epsilon}_i^p$, Equivalent plastic strain to damage initiation; $\bar{\epsilon}_f^p$, Equivalent plastic strain to failure; φ_{MBW} , Yield potential of the modified Bai-Wierzbicki model; γ , Parameter related to the Lode angle; μ , Friction coefficient; η , Stress triaxiality; η_c , Cut-off value of stress triaxiality; η_{avg} , Average stress triaxiality; σ_e , Equivalent stress; σ_m , Mean stress; σ_{yld} , Yield stress; σ_{y0} , Yield stress registered at the moment of damage initiation; $\bar{\sigma}(\bar{\epsilon}^p)$, Reference flow curve; $\sigma_1, \sigma_2, \sigma_3$, Principal stresses; τ , Friction stress; θ , Lode angle; $\bar{\theta}$, Normalised Lode angle parameter; $\bar{\theta}_{avg}$, Average Lode angle parameter
Abbreviations: BW, Bai-Wierzbicki; CDM, Continuum damage mechanics; DCPD, Direct current potential drop; DIL, Damage initiation locus; H/D, Height/diameter; JC, Johnson-Cook; MBW, Modified Bai-Wierzbicki

and fracture locus. The BW model has high accuracy, and its implementation procedures are simpler than those of micromechanical models. According to Besson,¹⁷ the BW model is an uncoupled model because it does not consider the effect of damage on the yield potential. Motivated by the complex interaction between damage and plasticity in modern high-strength steels, Lian et al proposed the modified Bai-Wierzbicki (MBW) damage model in a hybrid damage plasticity framework.¹⁸ The MBW model combines the BW phenomenological criterion for damage initiation related to the microstructure-level degradation of materials and a CDM-based damage evolution law for progressive damage accumulation until final fracture. With this modification, the model features a general and hybrid character that can be used to simulate various ductile failure processes in which damage plays a role.¹⁹ The MBW model has been successfully applied to simulations of the forming and machining of steels.^{20,21}

The stress state has a pronounced influence on damage evolution. Therefore, the strain history should be considered if loading paths are accompanied by varying stress states (non-proportional loading). Basu and Benzerga²² studied the path dependence of the fracture locus in ductile materials with a number of tensile tests subjected to varying loading paths and found that a stress-state-dependent critical fracture strain model is inadequate. Many approaches to consider the influence of non-proportional loading paths have been proposed. Material models, such as porous plasticity models, incorporate the damage variable and stress-state variables in the flow potential.⁴⁻⁸ Such models are able to follow complex loading states with varying load ratios due to their inherent failure criteria.²³ For strain-based material models, the Johnson-Cook (JC) model and BW model calibrate the fracture locus from tests with minor variations in the stress state and apply weighting schemes regarding the stress state to calculate the damage variable in modelling the non-proportional loadings.^{13,16} Bao and Wierzbicki investigated the fracture behaviour under high hydrostatic pressure and showed that the fracture does not occur under a cut-off value of stress triaxiality.¹⁴ Considering the cut-off value, Bao and Roland later presented a procedure to determine the weighting functions with respect to stress triaxiality for the damage evolution law. Such functions are important for loadings containing a precompression phase.²⁴ Aside from strain-based models, other criteria for modelling damage behaviour under complex loading conditions have also been presented in recent investigations. Derpenski and Seweryn²⁵ analysed the fracture initiation behaviour of a notched round bar specimen under complex torsion-tension conditions and proposed a damage criterion considering not only the strain but also the stress. Berto et al²⁶ applied an energy-based approach to simulate the damage behaviour of a notched specimen under torsion loading. Recent studies²⁷⁻²⁹ have suggested that not only the damage evolution law but also an accurate plasticity

description is important for modelling damage behaviour in complex loadings. Depending on the application, the advanced plasticity model may have to consider the stress state, anisotropy, and kinematic hardening to accurately describe the stress-strain behaviour of material under complex loading conditions.

As noted above, the MBW model considers stress triaxiality, the Lode angle parameter, and the damage-induced softening effect. However, it does not thoroughly consider the stress state and strain paths during damage evolution. This work proposes several necessary modifications to enhance the damage evolution law of the original MBW model and overcome the following drawbacks. The damage initiation locus (DIL) of the MBW model has the same problem identified by Benzerga²² for applications under complex loading conditions. In this work, the evaluation scheme for the damage initiation locus is modified to account for the stress-state variation, and a weighting scheme is added to the damage initiation locus to consider the progressive evolution of damage initiation under non-proportional loading conditions. In addition, previous CDM studies, such as the Lemaitre damage models,^{30,31} consider the stress triaxiality for calculating the evolution rate of the damage variable. In this study, the damage propagation after damage initiation is also changed to a stress-state-dependent scheme. The stress triaxiality and Lode angle parameter are formulated into the energy dissipation law, and a weighting scheme is used to account for the varying stress states in non-proportional loadings. Finally, the MBW model is proposed for a thin sheet material; thus, the aforementioned cut-off value phenomenon in the negative stress triaxiality range, which is often studied by compression testing, is not considered. According to Bao and Wierzbicki,¹⁴ this investigation applies a cut-off value to the damage evolution law to restrict the damage evolution under high hydrostatic pressure. The proposed damage mechanics model has simple phenomenological features and high computational efficiency compared to other micromechanical models. The classical uncoupled models, such as the JC and BW models, do not consider the damage initiation and damage-induced softening effect. The enhanced approach adopted the coupled approach of the MBW model, which is important for processes in which damage plays an important role. In addition, the enhanced model has indicators for damage initiation and failure, which can capture the progressive evolution of damage initiation and propagation under complex loading conditions.

At first, this paper introduces the original MBW model and proposes an enhanced damage evolution law for non-proportional loading conditions. Then, the experimental and simulation approaches for parameter calibration are presented. Finally, the extended material model is validated by two groups of experiments under non-proportional loading conditions.

2 | MATERIAL CHARACTERISATION

A normalised medium carbon steel is investigated in this work. The material is delivered as round bars with a diameter of 100 mm. The material has a ferritic-pearlitic microstructure.

The chemical composition was analysed at several locations in the cross section of the steel bar by spark emission spectrometry, and the mechanical properties were calibrated in a tensile test. The average values of the chemical composition and the characteristic values of mechanical properties are listed in Table 1.

Two tensile tests were performed on round bar specimens cut in different directions from the delivered steel bar to examine the anisotropy of the material. The stress-strain behaviour shown in Figure 1 indicates that the anisotropy of plasticity is negligible for the investigated material.

3 | MATERIAL MODEL

3.1 | Introduction of the MBW model

In isotropic materials, the stress states are typically characterised by the stress triaxiality η and Lode angle parameter $\bar{\theta}$. With the principal stresses denoted by σ_1 , σ_2 , and σ_3 , the invariants of the stress tensor p , q , and r and the two stress-state parameters η and $\bar{\theta}$ are defined as

$$p = -\sigma_m = -\frac{1}{3}(\sigma_1 + \sigma_2 + \sigma_3), \quad (1)$$

$$q = \sigma_e = \sqrt{\frac{1}{2} \cdot [(\sigma_1 - \sigma_2)^2 + (\sigma_2 - \sigma_3)^2 + (\sigma_3 - \sigma_1)^2]}, \quad (2)$$

$$r = \left[\frac{27}{2} \cdot (\sigma_1 - \sigma_m)(\sigma_2 - \sigma_m)(\sigma_3 - \sigma_m) \right]^{\frac{1}{3}}, \quad (3)$$

$$\eta = -\frac{p}{q}, \quad (4)$$

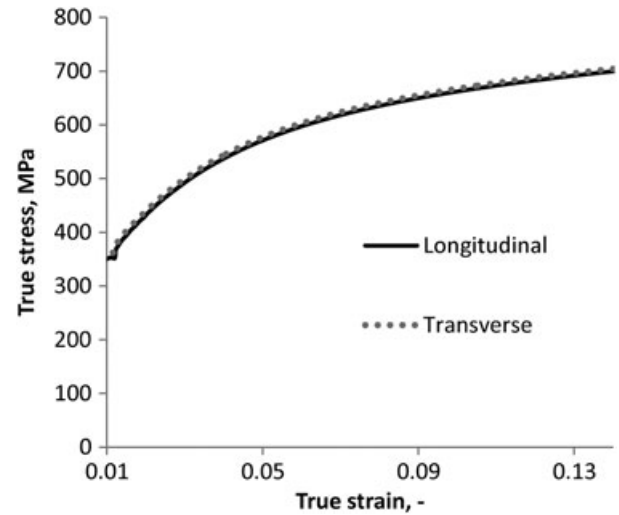


FIGURE 1 Flow curves of the C45E + N steel characterised by tensile tests performed on specimens cut from the steel bar in different directions

$$\bar{\theta} = 1 - \frac{2}{\pi} \arccos \left[\left(\frac{r}{q} \right)^3 \right]. \quad (5)$$

The original BW model addresses the influence of stress triaxiality and Lode angle parameter on the plasticity and the fracture behaviour of metals. Both the yield stress $\sigma_{yld}(\bar{\epsilon}^p, \eta, \bar{\theta})$ and fracture strain $\bar{\epsilon}_f^p(\eta, \bar{\theta})$ are formulated with respect to the two parameters. The MBW model was developed to properly describe the mechanical behaviour of newly developed steels, particularly high-strength steels, for which the impacts of damage on the strength and ductility are not negligible, and the accumulation of damage is dependent on the stress states. Readers are referred to Lian et al¹⁸ for the detailed equations and numerical implementation in ABAQUS. The yield potential of the MBW model is expressed as

$$\varphi_{MBW} = \sigma_e - (1 - D) \cdot \sigma_{yld}(\bar{\epsilon}^p, \bar{\theta}) \leq 0, \quad (6)$$

where σ_e is the equivalent stress; $\sigma_{yld}(\bar{\epsilon}^p, \bar{\theta})$ is the yield stress, which accounts for the strain hardening and the influence of the Lode angle parameter; and D is the damage variable. The

TABLE 1 Chemical composition and mechanical properties of the steel C45E + N

Chemical Composition (wt.%)								
C	Si	Mn	P	S	Cr	Ni	Al	Cu
0.45	0.18	0.60	0.018	0.027	0.07	0.03	0.016	0.10
Characteristic values of mechanical properties								
R _{eL} , MPa			R _{eH} , MPa		R _m , MPa		A _u	
324			331		566		15.3%	

damage-induced softening effect is coupled to the yield potential with the factor $(1-D)$.

The evolution of damage variable D is controlled by a damage initiation locus and a subsequent energy-based evolution law. It is equal to zero before damage initiation. The time instant of damage initiation during the mechanical tests can be calibrated by the direct current potential drop (DCPD) method. The calibration method was applied by Lian et al¹⁸ and Buchkremer et al²¹ for steels.

After damage initiation, the damage propagates according to an energy-based linear evolution law, which is given as follows:

$$D = \begin{cases} 0; & \bar{\epsilon}^p \leq \bar{\epsilon}_i^p \\ \int_{\bar{\epsilon}_i^p}^{\bar{\epsilon}^p} \frac{\sigma_{y0}}{G_f} d\bar{\epsilon}^p; & \bar{\epsilon}_i^p < \bar{\epsilon}^p < \bar{\epsilon}_f^p, \\ D_{cr}; & \bar{\epsilon}_f^p = \bar{\epsilon}^p \end{cases} \quad (7)$$

where G_f is the energy dissipation parameter; σ_{y0} is the yield stress to damage initiation; $\bar{\epsilon}_i^p$ is the stress-state-dependent damage initiation strain; $\bar{\epsilon}_f^p$ is the strain to failure; and D_{cr} is the critical damage variable to fracture.

The final ductile fracture is triggered when the damage accumulation reaches a critical value D_{cr} . Figure 2 shows the stress-strain behaviour of a material described by the MBW model.

As discussed in the introduction, the MBW model has some significant shortcomings in modelling damage behaviour under non-proportional loading conditions. The cut-off value in the negative stress triaxiality range, which is often studied by compression testing, is not considered. In addition, the calibration of the damage initiation strain $\bar{\epsilon}_i^p$ is based on the presumption of proportional loading. The variation of the stress state during calibration and application is not considered. Furthermore, in Equation 7, the energy-based evolution law for damage propagation is described by a single set of values (G_f and D_{cr}), which do not adequately consider the stress states and complex strain paths that occur during damage propagation.

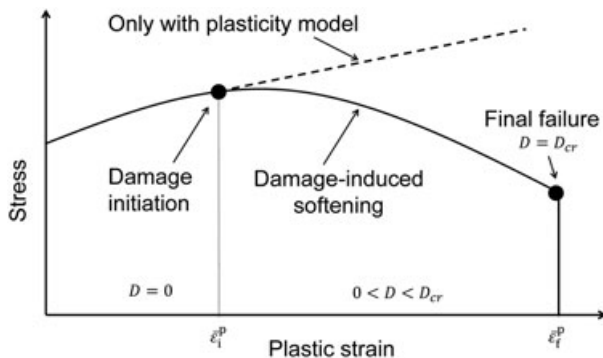


FIGURE 2 Schematic representation of the stress-strain behaviour described by the modified Bai-Wierzbicki model

3.2 | Enhanced MBW model for complex loading conditions

This work proposes an enhanced MBW model for complex loading conditions with varying stress states. The MBW model is significantly modified to consider the influence of the stress state and to capture the progressive damage evolution during non-proportional strain paths. It should be noted that this work only considers failure processes subjected to non-proportional strain paths that occur under macroscopic monotonic loading conditions, in which the effect of kinematic hardening can be neglected. The presented model adopts the plasticity description and the coupled approach of the MBW model and focuses on the development of the damage evolution law. The enhanced MBW model is explained in detail below.

3.2.1 | Plasticity model

As discussed in the introduction, an accurate description of the plasticity is important for the modelling of ductile fracture under complex loading conditions. The experiment results presented in Figure 1 show that the material is isotropic. Our investigation is limited to applications of loading conditions under which kinematic hardening can be neglected. Therefore, we only consider the influence of the stress state on the plasticity. Many previous studies (e.g., Bai and Wierzbicki,¹⁶ Hosford,³² Karafillis, and Boyce³³) have formulated non-quadratic yield functions to account for the effect of the stress state on plastic deformation. Here, an isotropic plasticity description following the MBW model that considers the influence of the Lode angle dependence is implemented. The plasticity rule of the MBW model is based on the more generalised non-quadratic plasticity rule of the BW model and neglects the trivial influence of stress triaxiality for steels. The Lode-dependent plasticity description of this model is advantageous in that it can represent an asymmetric yield surface for uniaxial tension and uniaxial compression in the deviatoric stress plane. In addition, the model parameters have physical meanings corresponding to different stress states. The yield potential of the proposed coupled damage mechanics model for applications at quasi-static loading rates and room temperature is expressed as¹⁸

$$\begin{aligned} \varphi_{MBW} &= \sigma_e (1-D) \cdot \sigma_{yld}(\bar{\epsilon}^p, \bar{\theta}) \\ &= \sigma_e (1-D) \cdot \bar{\sigma}(\bar{\epsilon}^p) \cdot \left[c_\theta^s + (c_\theta^{ax} - c_\theta^s) \cdot \left(\gamma - \frac{\gamma^{m+1}}{m+1} \right) \right] \leq 0, \end{aligned} \quad (8)$$

$$\text{with } \gamma = \frac{\cos(\frac{\pi}{6})}{1 - \cos(\frac{\pi}{6})} \left[\frac{1}{\cos(\frac{\pi}{6})} - 1 \right] = 6.4641 \left[\sec(\theta - \frac{\pi}{6}) - 1 \right] \text{ and}$$

$$c_{\theta}^{ax} = \begin{cases} c_{\theta}^t & \text{for } \bar{\theta} \geq 0 \\ c_{\theta}^c & \text{for } \bar{\theta} < 0 \end{cases},$$

- σ_e : von Mises equivalent stress,
 $\bar{\sigma}(\bar{\epsilon}^p)$: reference flow curve, determined by a quasi-static tensile test at room temperature,
 $c_{\theta}^s, c_{\theta}^c, c_{\theta}^t, m$: model parameters for the correction factor of the stress state,
 D : damage variable.

The term $f(\bar{\theta}) = c_{\theta}^s + (c_{\theta}^{ax} - c_{\theta}^s) \cdot \left(\gamma - \frac{\gamma^{m+1}}{m+1} \right)$ is the correction factor of the yield stress for the Lode angle parameter.

3.2.2 | Modified damage evolution law for complex loading conditions

The coupled plasticity-damage approach based on the MBW model is implemented. A multiplier $(1-D)$ in the yield potential is used to describe the damage-induced softening effect. This study significantly modifies the damage evolution law of the MBW model for complex loading conditions because the previously introduced MBW model does not consider the complex strain history and damage behaviour under extremely low stress triaxialities. The hypotheses behind the modifications are as follows: The damage evolution is suppressed when the stress triaxialities are below the cut-off value; the damage propagation after damage initiation is dependent on the stress triaxiality and Lode angle parameter; and the damage evolution under non-proportional loading conditions can be described by linear weighting schemes with consideration of the stress state parameters. This work makes several modifications to enhance the original MBW model based on these hypotheses. First, a cut-off value is introduced into the material model to describe the material behaviour under high hydrostatic pressures. Second, a stress-state-dependent damage propagation law is applied. Third, weighting schemes are implemented in the evolution laws for damage initiation and propagation to consider the non-proportional loading paths. The details of the damage evolution are provided below.

As illustrated in Figure 3, damage evolution is assumed to be a continuous process from the beginning of plastic deformation. After damage initiation, i.e., the formation of micro cracks in the material, the damage evolution accelerates. The damage evolution can be divided into two phases with a linear approximation. The end of the first phase denotes the beginning of damage initiation, and the end of the second line represents the failure. In this study, a damage initiation indicator D_i and failure indicator D_f are proposed to describe the evolution of damage initiation and failure, respectively. A damage initiation locus and an energy-based damage evolution law as well as corresponding weighting

schemes based on the stress state are applied to calculate these two indicators. Damage initiation and failure are supposed to occur when D_i and D_f reach one, respectively.

Cut-off value in negative stress triaxiality

Bao and Wierzbicki¹⁴ analysed the results of many mechanical tests and found that fracture does not occur under very low stress triaxiality. By investigating the fracture locus in the principal strain space obtained from upsetting tests, they proposed an analytical equation to describe the influence of stress triaxiality on failure strains. The analytical equation shows that the failure strain tends to be infinite when the stress triaxiality approaches $-1/3$. Based on this investigation, they proposed a cut-off value $\eta_c = -1/3$ for metals. Their work reveals an important feature of fracture: When metals are subject to deformation under stress triaxialities below this value, the damage evolution is supposed to be fully suppressed by the high hydrostatic pressure. They proved this analytically derived value by analysing a series of tensile tests performed on tensile specimens under high hydrostatic pressures. Fracture was not identified in these tests under a stress triaxiality of $-1/3$. In addition, they simulated the tests on C45 (AISI 1045) steel and further verified the postulated cut-off value. The concept of cut-off value was later confirmed and applied by Teng and Wierzbicki,³⁴ Lou et al.,³⁵ and Wu et al.³⁶ The cut-off value is particularly important for forming processes, in which the material is deformed to a large extent under low negative stress triaxiality, thus causing the fitting and extrapolation of experimental data from the higher stress triaxiality range to low stress triaxiality range no longer be valid. In this investigation, the same cut-off value of $\eta_c = -1/3$ is integrated in the damage

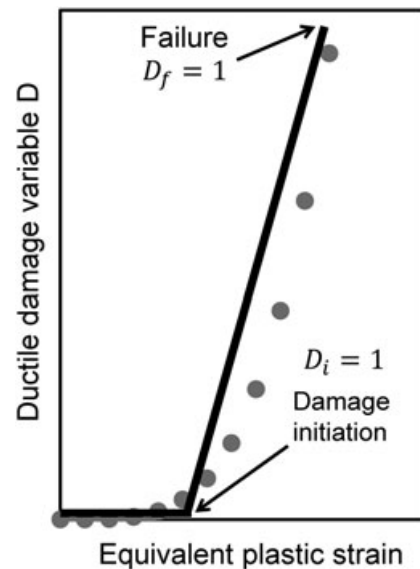


FIGURE 3 Schematic representation of the linear approximation of damage evolution

evolution law of the material model. It is assumed that the damage evolution is completely suppressed when the stress triaxiality is less than $-1/3$.

Damage initiation criterion

The original MBW model assumes an instant damage initiation criterion, i.e., the damage initiates once the critical strain is reached under a certain stress state without considering the loading history. This assumption is maintained only for the proportional loading condition. However, under non-proportional loading conditions, this instant criterion may lead to deviation of the failure prediction. Considering the variation of stress states in calibration and applications, modifications are necessary.

As shown in Figure 4, although the mechanical test is designed to generate proportional loading conditions in the specimen, the geometries of the shear specimen vary within a small range during loading, and the stress states change correspondingly.

Because the stress state is not constant throughout the entire test, the average values of the stress-state parameters are used for evaluation in this study. The average values of stress triaxiality and the normalised Lode angle parameter are calculated according to Equations 9 and 10, respectively:

$$\eta_{avg} = \int_0^{\bar{\epsilon}_i^p} \frac{\eta d\bar{\epsilon}^p}{\bar{\epsilon}_i^p}, \quad (9)$$

$$\bar{\theta}_{avg} = \int_0^{\bar{\epsilon}_i^p} \frac{\bar{\theta} d\bar{\epsilon}^p}{\bar{\epsilon}_i^p}. \quad (10)$$

The DIL can be derived with the extracted values of $\bar{\epsilon}_i^p$ (η_{avg} , $\bar{\theta}_{avg}$) in different tests under a wide range of stress states. This equation of DIL is inspired by the function of fracture locus proposed by Bai and Wierzbicki,¹⁶ who extended the classical JC model with Lode dependence. In the widely applied JC model, the damage curve can be

described by a hyperbolic equation regarding the stress triaxiality. Instead of the strain to failure, the DIL describes the damage initiation strains with respect to the two stress-state parameters. The damage initiation strain is assumed to be a hyperbolic function regarding the stress triaxiality and symmetric with respect to the normalised Lode angle parameter. The function of the DIL is given as

$$\bar{\epsilon}_i^p = [C_1 e^{-C_2 \eta} - C_3 e^{-C_4 \eta}] \bar{\theta}^2 + C_3 e^{-C_4 \eta}, \quad (11)$$

where C_1 - C_4 are model parameters.

For proportional loading in which the stress-state parameters η and $\bar{\theta}$ are constant throughout the entire loading process, the damage initiation occurs when the accumulated plastic strain reaches $\bar{\epsilon}_i^p(\eta, \bar{\theta})$ according to the DIL in Equation 11. To describe the progressive evolution of damage initiation for non-proportional loading conditions, a weighting function is required to account for the different effects on damage initiation for strain increments accumulated under varying stress states. An indicator D_i for damage initiation is used. The increment of D_i in step n is calculated as

$$\Delta D_{i,n} = \begin{cases} \frac{\Delta \bar{\epsilon}_n^p}{\bar{\epsilon}_{i,n}^p(\eta_n, \bar{\theta}_n)}; & \eta > \eta_c, \\ 0; & \eta \leq \eta_c \end{cases}, \quad (12)$$

where $\Delta \bar{\epsilon}_n^p$ is the strain increment in step n ; $\bar{\epsilon}_{i,n}^p(\eta_n, \bar{\theta}_n)$ is the strain to damage initiation for the stress state in step n ; and η_c is the cut-off value of stress triaxiality, below which the damage evolution is suppressed. The value of D_i increases monotonically, and damage is initiated when $D_i = \sum \Delta D_i$ reaches one.

3.2.3 | Damage propagation after damage initiation

After damage initiation occurs, the damage begins to propagate. An energy-based evolution rule is used to describe the damage propagation in this investigation. The increment of damage variable in step n is expressed as

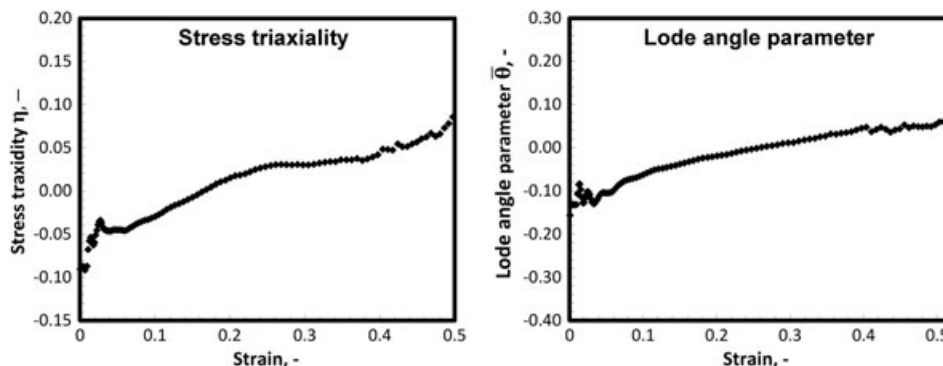


FIGURE 4 Variation of the stress-state parameters during a shear test

$$\Delta D_n = \begin{cases} 0 & ; \quad D_i < 1 \\ \frac{\sigma_{y0}}{G_f} \Delta \bar{\epsilon}_n^p & ; \quad D_i = 1 \wedge \eta > \eta_c \\ 0 & ; \quad D_i = 1 \wedge \eta \leq \eta_c \end{cases} \quad (13)$$

where σ_{y0} is the yield stress to damage initiation, and G_f is the energy-dissipation parameter. The damage variable $D = \Sigma \Delta D$ is the summation of all of the damage increments. Before damage initiation ($D_i < 1$), the damage variable is zero. The cut-off value is used to restrict the damage evolution under high hydrostatic pressure. The damage propagation is assumed to stop when $\eta_c \leq -1/3$. Under a certain stress state during proportional loading, the parameter G_f controls the rate of damage accumulation and thus also controls the softening rate of material. The material is assumed to completely fail when the damage variable D reaches a critical value D_{cr} . However, by using a single parameter set of G_f and D_{cr} derived from one mechanical test, the damage variable evolves independently from the stress state. In this study, the energy dissipation law of the MBW model is modified to be dependent on the stress state. Both the stress triaxiality and Lode angle parameter influence the damage propagation governed by G_f and D_{cr} . To simplify the model, G_f is assumed to be constant, and $D_{cr}(\eta, \bar{\theta})$ is set to be dependent on the stress state. The critical damage value $D_{cr}(\eta, \bar{\theta})$ can be calibrated by analysing the failure behaviour of a series of proportional loading experiments encompassing a wide range of stress states. Analogous to the damage initiation locus, the dependence of D_{cr} on the stress-state parameters is assumed to be described by the same type of function, namely,

$$D_{cr} = [C_5 e^{-C_6 \eta} - C_7 e^{-C_8 \eta}] \bar{\theta}^2 + C_7 e^{-C_8 \eta}, \quad (14)$$

where C_5 – C_8 are model parameters.

TABLE 2 Equations for the damage evolution law

Damage Initiation	
$\bar{\epsilon}_i^p = [C_1 e^{-C_2 \eta} - C_3 e^{-C_4 \eta}] \bar{\theta}^2 + C_3 e^{-C_4 \eta}$	Damage initiation locus
$\Delta D_{i,n} = \begin{cases} \frac{\Delta \bar{\epsilon}_n^p}{\bar{\epsilon}_{i,n}^p(\eta_n, \bar{\theta}_n)} & ; \quad \eta > \eta_c \\ 0 & ; \quad \eta \leq \eta_c \end{cases}$	Evolution law for the damage initiation indicator D_i : the increment of the damage initiation indicator in step n
$D_i = \Sigma \Delta D_i$	Damage initiation takes place when $D_i = 1$
Damage propagation	
$\Delta D_n = \begin{cases} 0 & ; \quad D_i < 1 \\ \frac{\sigma_{y0}}{G_f} \Delta \bar{\epsilon}_n^p & ; \quad D_i = 1 \wedge \eta > \eta_c \\ 0 & ; \quad D_i = 1 \wedge \eta \leq \eta_c \end{cases}$	Evolution law of the damage variable: the increment of damage variable in step n
$D_{cr} = [C_5 e^{-C_6 \eta} - C_7 e^{-C_8 \eta}] \bar{\theta}^2 + C_7 e^{-C_8 \eta}$	Locus for the critical value of damage variable
$D_f = \Sigma \frac{\Delta D_n}{D_{cr}(\eta_n, \bar{\theta}_n)}$	Evolution law of the failure indicator Failure takes place when $D_f = 1$

A failure indicator is used to account for non-proportional loading conditions in this work. The effects of damage increments on the failure are weighted according to the stress state. The failure indicator is calculated by summing the weighted damage increments:

$$D_f = \Sigma \frac{\Delta D_n}{D_{cr}(\eta_n, \bar{\theta}_n)}, \quad (15)$$

where $D_{cr}(\eta_n, \bar{\theta}_n)$ is the critical damage value under the stress state $(\eta_n, \bar{\theta}_n)$ in step n . When the failure indicator D_f reaches one, the material completely loses its stiffness, and the corresponding element is removed from the numerical analysis.

This study significantly modified the damage evolution law of the MBW model. The proposed damage model consists of criteria for damage initiation and damage propagation. The equations are summarised in Table 2.

4 | EXPERIMENTS

Various mechanical tests were performed to study the damage evolution under different stress states and loading histories. Figure 5A–D shows two notched round bar specimens with different notch radii, a round bar specimen, two flat grooved specimens with different notch radii, and a shear sample, respectively. Tensile tests were performed on these specimens. Figure 5E–G shows the specimens used in the compression tests. Friction significantly influences the results of compression tests. Therefore, ring specimens, shown in Figure 5E, were used to calibrate the friction coefficient according to the method described by Silva et al.³⁷ A Rastegaev specimen with recesses is shown in Figure 5F. Lubricant can be filled in the recesses to minimise the barreling effect during the test. During a compression test without the occurrence of barreling, the sample is subject to a stress

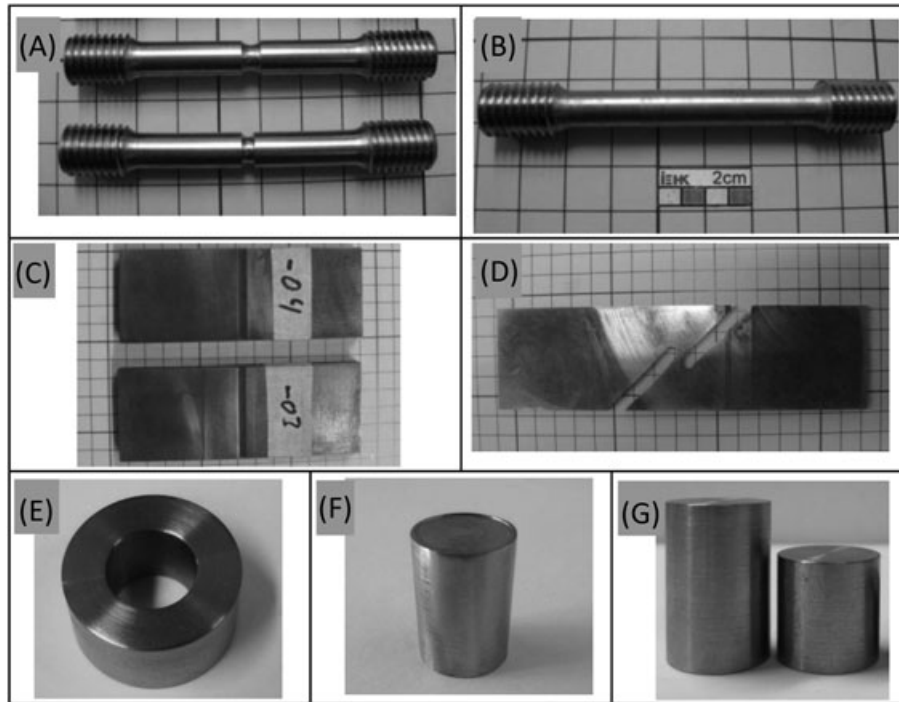


FIGURE 5 A, Notched round bar specimens with notch radii of 3 and 5 mm; B, smooth round bar specimen; C, flat grooved specimens with notch radii of 3 and 5 mm; D, shear specimen; E, ring specimen; F, Rastegaev specimen; and G, cylindrical specimens

state of $\bar{\theta} = -1$ and $\eta = -1/3$. This stress state is used to study the material behaviour under high hydrostatic pressure and to validate the presumption of the cut-off value. Figure 5 G shows two cylindrical specimens with different ratios of height/diameter (H/D). All of the aforementioned tests were performed under quasi-static conditions at a loading rate of 0.2 mm/min.

Among the conducted mechanical tests, a two-step tensile test and a set of compression tests under complex non-proportional loading conditions are introduced in detail here. The two-step tensile test is illustrated in Figure 6A. In the first step, the round bar specimen shown in Figure 5B was loaded under uniaxial tension until a total strain of 15% was reached. Because necking does not occur during preloading, the stress state is $\bar{\theta} = 1$ and $\eta = 1/3$. Then, a notch with a radius of 3 mm and a depth of 1 mm was manufactured in the middle of the prestrained sample. Finally, the notched round bar specimen was further loaded until fracture. Due to the notch effect, the stress triaxiality increases from 1/3 to a larger value. The other set of non-proportional loading tests were performed on the specimens shown in Figure 5G. The compression tests were conducted on the round bar specimens without using lubricants. As shown in Figure 6 B, during the compression test, the friction between the specimen and contact plates of testing machining results in barrelling. After barrelling occurs, the stress state deviates from the uniaxial compression, and both the stress triaxiality and Lode angle parameter vary continuously in the region near the barrelling surfaces. Therefore, the material at the

surfaces of the specimens is subject to complex loading paths. Specimens with different H/D ratios were studied in the experiments because the H/D ratio influences the

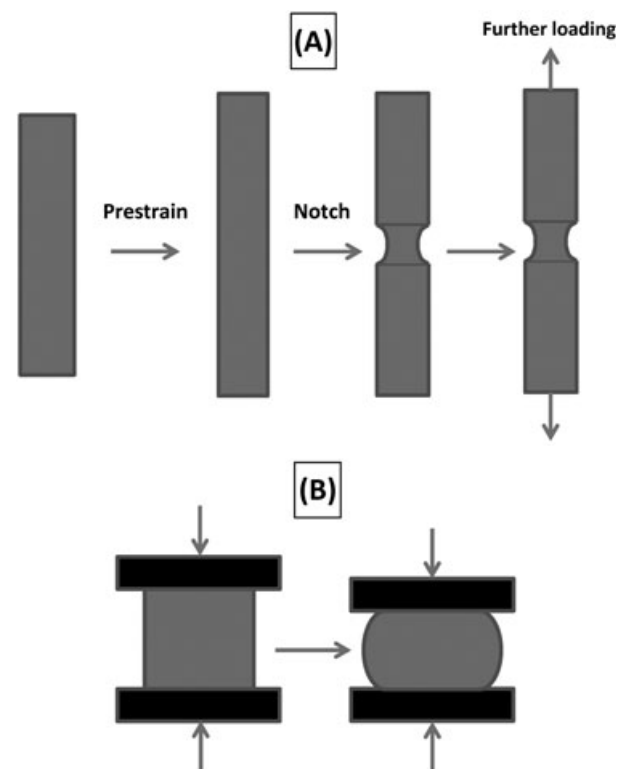


FIGURE 6 A, Two-step tensile test and B, Barrelling of a cylindrical specimen in compression test performed without using lubricant

evolution of the stress state at the surface of the specimen when barrelling occurs.

5 | FE MODEL

The simulation models of different tests are shown in Figure 7. Due to symmetry, only one-eighth of the model was created for tensile tests performed on round bar, notched round bar, and flat grooved samples, illustrated in Figure 7A, C, respectively. A full model for the shear test is presented in Figure 7B. One quarter of the model was built for the compression tests with different H/D ratios for better visualisation of the crack morphology. As shown in Figure 7D, the model for the compression tests consists of two analytical plates and a deformable cylindrical specimen. The friction properties can be defined between the contact surfaces. The FE model is more complex for the two-step tensile test. In the second loading step, the change of material properties induced from the first loading step is predefined in the model.

The proposed material model was programmed as a VUMAT subroutine for the commercial code ABAQUS/Explicit. The material model used for the simulations is implemented with local formulations. Therefore, it suffers from mesh dependence, and a consistent mesh is necessary for all of the FE models. Eight-node linear brick elements with reduced integration formulation (C3D8R) were used for all of the simulation models. A fine mesh size of 0.15 mm was used in the models for the round bar tension tests and round bar compression tests. For the models of

the notched round bar, flat grooved samples, and shear test, a fine mesh with the mesh size of 0.15 mm was used in the critical regions of the models. A coarser mesh was used in other parts of the models to reduce the cost of the numerical analyses. In addition, time scaling was used in all of the simulations to reduce the calculation time.

6 | PARAMETER CALIBRATION

Due to the significant modifications, we introduced many additional parameters into this model, which increases the difficulty of calibration and numerical implementation. However, the experiments used for calibration are the same as before, and only the numerical procedures for calibration need to be modified.

6.1 | Parameter calibration for the plasticity description

The plasticity part of this model is adopted from the MBW model, and the parameters are taken from a previous work for the same material.²¹ The reference flow curve was derived from a uniaxial tension test. The influence of the stress state on plasticity was studied by shear and compression tests. The parameters $c_\theta^s = 0.95$, $c_\theta^c = 0.98$ and $m = 7$ for the correction factor of the Lode angle parameter were applied in this investigation.

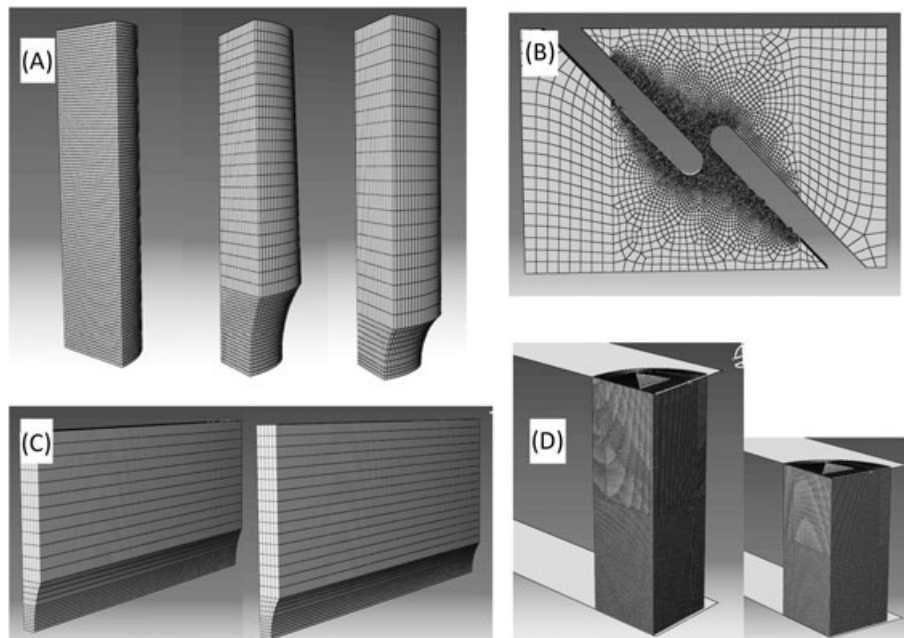


FIGURE 7 FE simulation models. A, Round bar and notched round bars with different notch radii; B, shear sample; C, flat grooved samples with different notch radii; and D, compression test samples with different H/D ratios

6.2 | Parameter calibration for the damage evolution law

6.2.1 | Validation of the cut-off value

The cut-off value proposed by Bao and Wierzbicki was already proven in experiments and simulations for a similar C45 steel.¹⁴ In this investigation, a Rastegaev compression test was performed on a cylindrical sample with lubricant to validate the assumption. The specimen was loaded during a uniaxial compression test until a large strain of 1.5 occurred; however, a crack does not form at the surface, as shown in Figure 8. The experiment was stopped because the testing machine already reached its force limit. In addition, the recesses filled with lubricant were also broken due to the extremely high pressure applied in the last phase of the test. Therefore, it was not meaningful to continue the test because the barrelling increased the stress triaxiality at the surface of the compression specimen to a value greater than the cut-off value. Under a stress triaxiality of $-1/3$, the material exhibited unusually high ductility; therefore, the cutoff value postulated by Bao and Wierzbicki is proven to be reasonable for the investigated material.

6.2.2 | Damage initiation locus

Mechanical tests coupled with the DCPD method and numerical simulations were applied to calibrate the DIL. Readers are referred to Lian et al¹⁸ for details on this method. As discussed in the damage initiation criterion section, the stress state is not constant during the mechanical tests. This work modifies the evaluation method for calibrating the DIL. The stress-state variables η_{avg} and $\bar{\theta}_{avg}$ were calculated according

to Equations 9 and 10, respectively. The time instant of damage initiation in the shear, uniaxial tension, plane strain tension, and notched round bar tension tests were calibrated with the DCPD method. In the numerical analysis, the equivalent plastic strain $\bar{\epsilon}_i^p$ at the instant of damage initiation and the histories of strain increments and stress-state parameters were extracted from the element at the location of damage initiation for each test. The damage initiation behaviour under a wide range of stress states can be investigated by studying a series of proportional tests (tensile tests performed on round bars, notched round bars, and flat grooved specimens as well as shear tests). The DIL is fitted using six experimental data according to Equation 11 and is given as follows:

$$\bar{\epsilon}_i^p = [0.4943e^{-2.266\eta} - 0.2683e^{-1.131\eta}] \bar{\theta}^2 + 0.2683e^{-1.131\eta}. \quad (16)$$

6.2.3 | Damage propagation

G_f and D_{cr} are related to the damage propagation after damage initiation. These two parameters can be calibrated by iteratively fitting the force-displacement curves of simulations to the experimental results. Figure 9 shows the calibration procedure of G_f and D_{cr} for a plane strain tension test. A flat grooved sample with a notch radius $R=5$ mm shown in Figure 5C was investigated. First, G_f was calibrated by comparing the softening rate, and then, D_{cr} was derived by fitting the time instant of failure.

However, the calibrated G_f and D_{cr} are only valid for the corresponding stress state in the plane strain tension test.

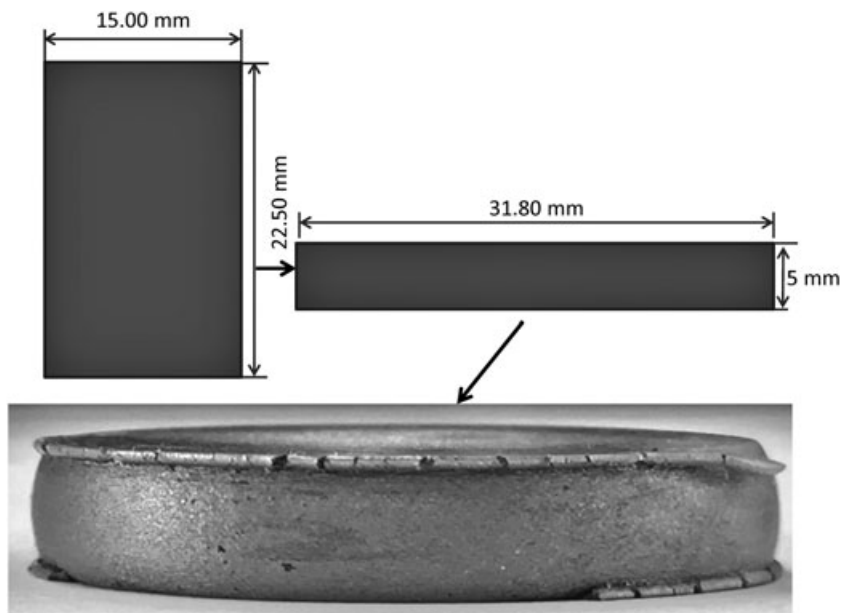


FIGURE 8 Result of the Rastegaev compression test

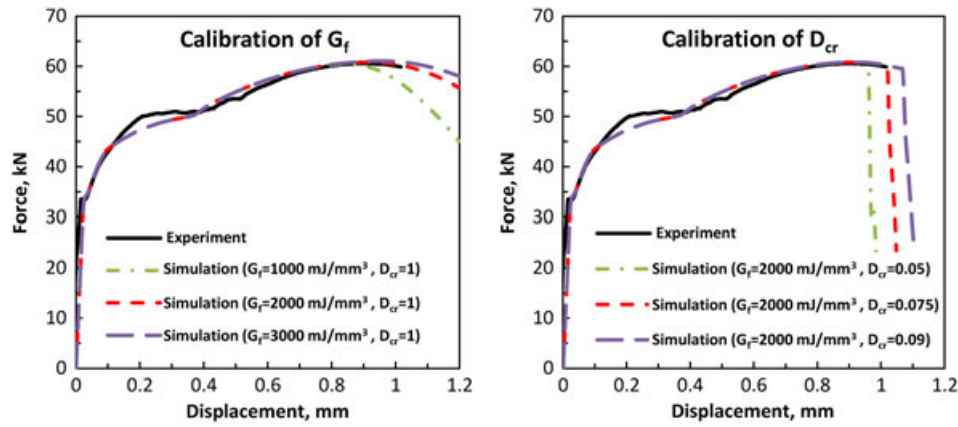


FIGURE 9 Calibration of G_f and D_{cr} for a plane strain test [Colour figure can be viewed at wileyonlinelibrary.com]

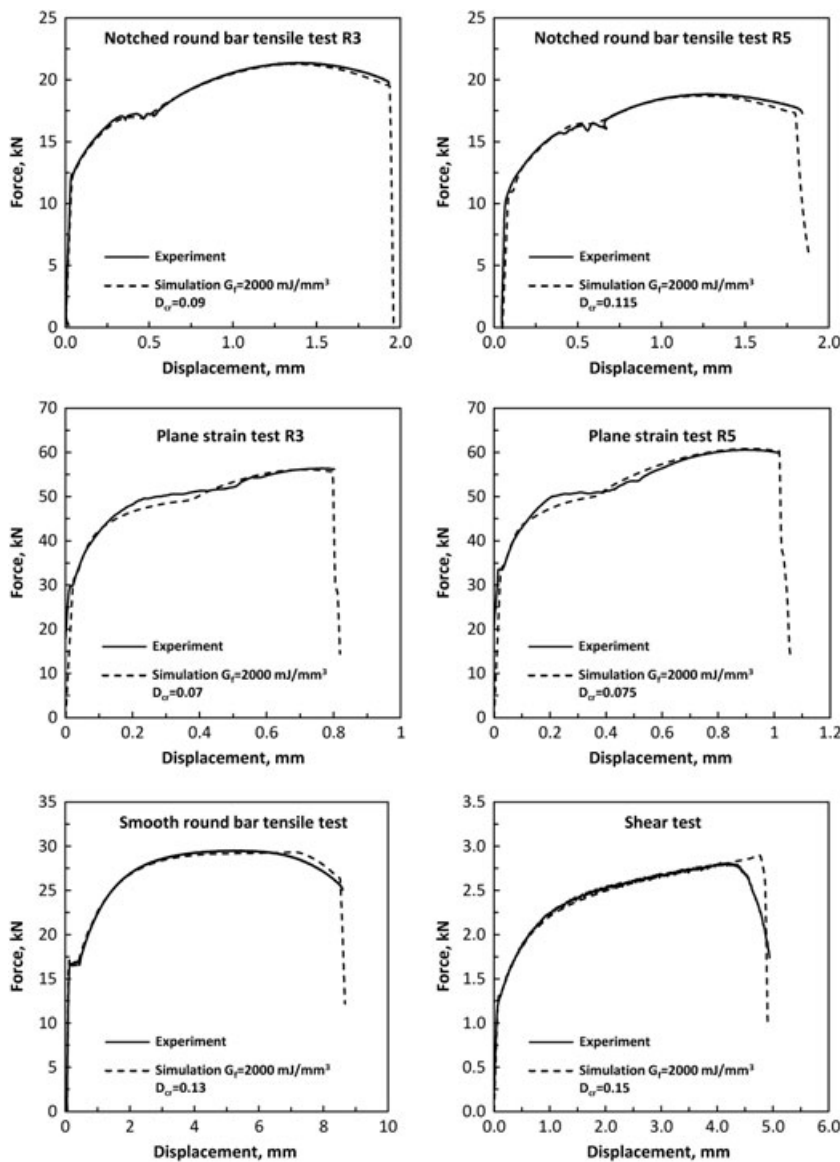


FIGURE 10 Force-displacement curves for the calibrated values of damage variable D_{cr}

Lian et al noted that a single set of scalar values of these two parameters cannot result in a consistently accurate prediction of the final fracture for all stress states.¹⁸ Thus, the damage

propagation after damage initiation is also dependent on the stress state, and different parameter sets are required to describe the energy dissipation during fracture. Modification

of the D_{cr} from a scalar value to a function dependent on the Lode angle parameter was performed in several previous studies^{38,39} and improved the prediction of final fracture considerably. In this work, the approach is further developed. The dependence of the energy dissipation on both the stress triaxiality and Lode angle parameter during damage propagation is considered in the proposed damage evolution law in terms of D_{cr} . $G_f = 2,000 \text{ mJ/mm}^3$ was assumed for all of the tests under various stress states, and D_{cr} was fitted in the simulations for the other tests. The failure behaviour can be accurately simulated by applying different D_{cr} values during these proportional loading tests under different stress states. The calibrated values of D_{cr} for different tests are given in Figure 10.

Similar to the extraction procedures for determining the damage initiation locus, the evolution histories of the stress-state parameters and strain increments were also extracted,

and the local values of η_{avg} and $\bar{\theta}_{avg}$ can be derived for all of the tests presented in Figure 10. Using these data, a D_{cr} locus is fitted according Equation 14 as follows:

$$D_{cr} = (0.1675e^{-0.5449\eta} - 0.143e^{-0.9263\eta})\bar{\theta}^2 + 0.143e^{-0.9263\eta}. \quad (17)$$

The R-square values of the surface fitting are 0.95 and 0.98 for the DIL and the D_{cr} locus, respectively, which indicates the high quality of the surface fitting results.

6.3 | Modelling of the proportional loadings with the calibrated material model

The derived material model was applied to simulations of the calibration tests in which the material is subject to quasi-proportional loadings. As shown in Figure 11, the simulated

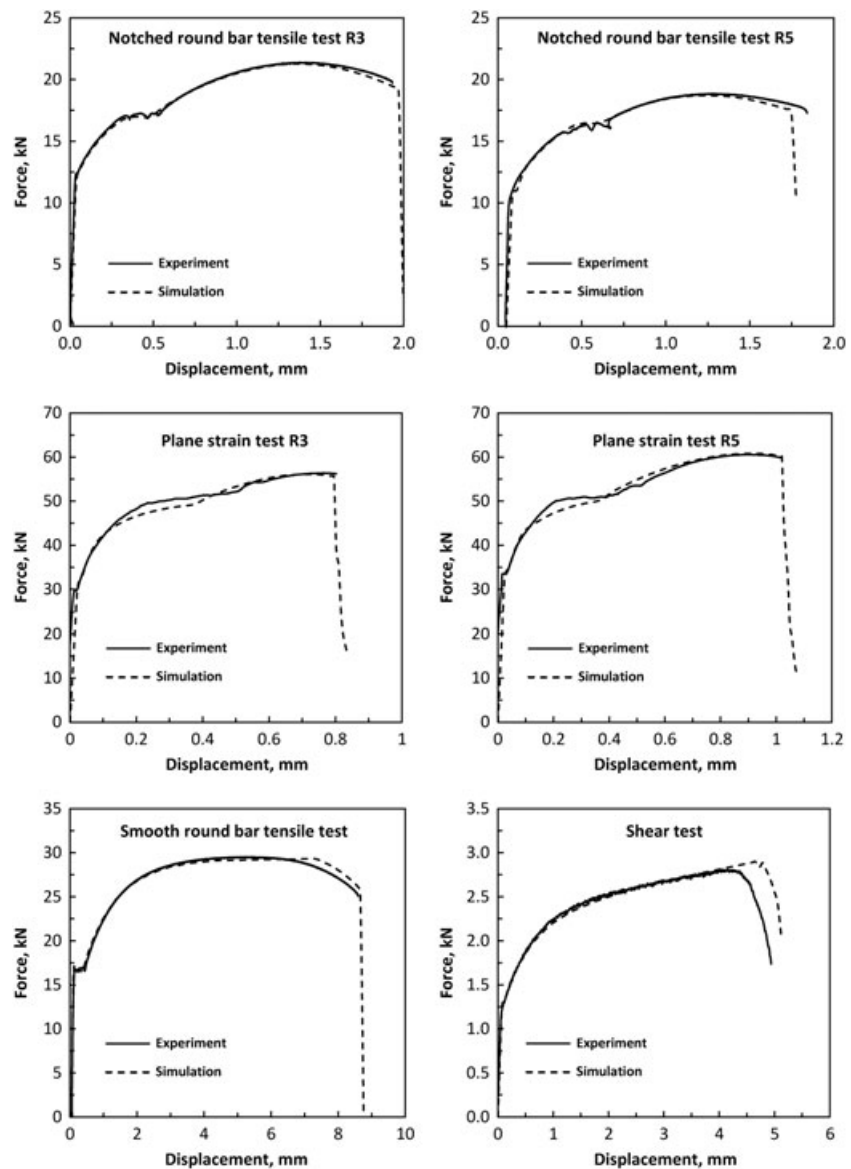


FIGURE 11 Modelling of the mechanical tests under proportional loading conditions

force-displacement curves correspond well with the experimental results. Slight deviations are found in the comparison for the notched round bar tensile test R5 and shear test. The errors could be induced from the deviation in the surface fitting. The good agreement demonstrates the high quality of the surface fitting for damage initiation locus and D_{cr} locus. The modified evaluation method for the stress-state parameters and supplemented evolution laws also contribute to the accuracy of the predictions. The proposed model is able to capture the damage behaviour of quasi-proportional loadings under a wide range of stress states.

7 | VALIDATION OF THE PROPOSED MODEL WITH TESTS UNDER COMPLEX LOADING PATHS

Two types of non-proportional tests presented in Section 4 were used to validate the applicability of the material model under complex loading conditions.

7.1 | Validation with two-step tensile test

After loading the round bar specimen to a strain of 15%, a notch was manufactured in the middle of the sample. The prestrain level is below the uniform strain, i.e., necking does not occur. Then, the specimen was loaded until fracture in the

second step. As illustrated in Figure 12A, the round bar sample is subject to uniaxial tension ($\eta=1/3$, $\bar{\theta}=1$) in the first step of the tensile test. In the second step, the stress triaxiality in the sample increases to a value of approximately 1.2 due to the notch effect, and the value of the Lode angle parameter remains at one. Figure 12B shows a comparison of the force-displacement curves for the second loading step of the test. Although the stress triaxiality increases during the two-step tension test, the proposed model successfully predicts the failure behaviour.

7.2 | Validation with compression tests

Compression tests were performed on cylindrical specimens to validate the model. To study the compression test under dry lubrication conditions, the friction coefficient should be calibrated first. A constant friction model $\tau=\mu k$ was assumed at the contact surface between the compression specimens and the plates of the testing machine. As shown in Figure 13, the friction coefficient was estimated by comparing the change in the internal diameter and the reduction in height between the experiments and FE simulations. In the FE simulations, different friction coefficients were applied and the calibrated curves were plotted together with the experimental results. A friction coefficient of 0.35 was determined using this approach.

Due to the existence of friction, a triaxial stress state as a result of the barrelling effect occurs instead of uniaxial compression ($\eta=-1/3$, $\bar{\theta}=-1$) in the Rastegaev compression test. The simulation result for one compression test is illustrated in Figure 14. The initial stress state at the outer surface is $\eta=-1/3$ and $\bar{\theta}=-1$. Both the stress triaxiality and Lode angle parameter increase after barrelling occurs. The inner part is severely compressed under stress triaxialities of less than $-1/3$. Figure 14 also shows the distribution of the failure indicator value and the evolution of the stress-state parameters. Because of symmetry, only one quarter of the model is created, and half of the cross section is shown in the figure. The evolution of the stress-state parameters in the centre of the specimen shows that the value of the Lode angle parameter remains at a constant value of negative one during modelling, and the value of stress triaxiality is less than $-1/3$. Therefore, the cut-off value concept integrated in the material model restricts the damage evolution in this region. In the major inner region of the compression sample, the stress triaxiality is less than the cut-off value, and the failure indicator remains at zero. In contrast, the outer barrelling surface experiences complex strain paths with continuous varying triaxial stress states, and the more critical stress state results in crack initiation first at the outer barrelling surface. Both of the stress-state parameters vary considerably at the outer surface. It is subject to a continuous stress-state change from

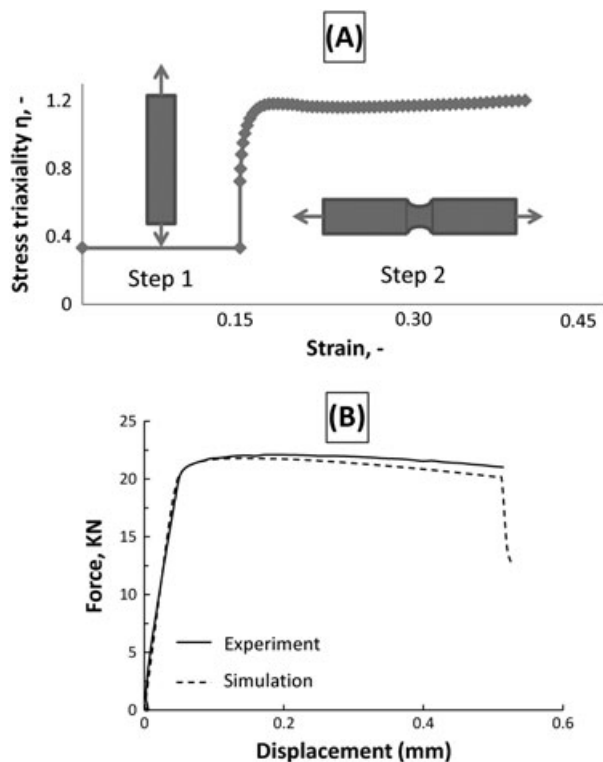


FIGURE 12 A, Evolution of stress triaxiality during a two-step tensile test and B, Force-displacement curves of the two-step tensile tests (second step)

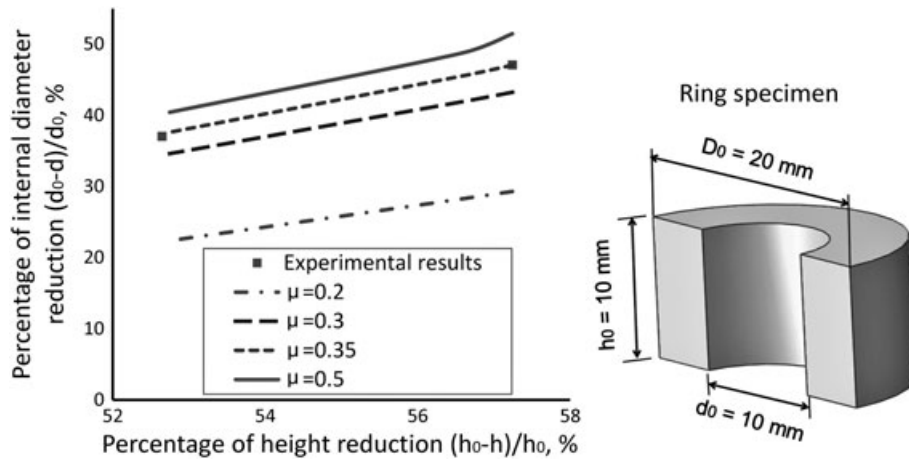


FIGURE 13 Characterisation of the friction coefficient with ring tests and FE simulation

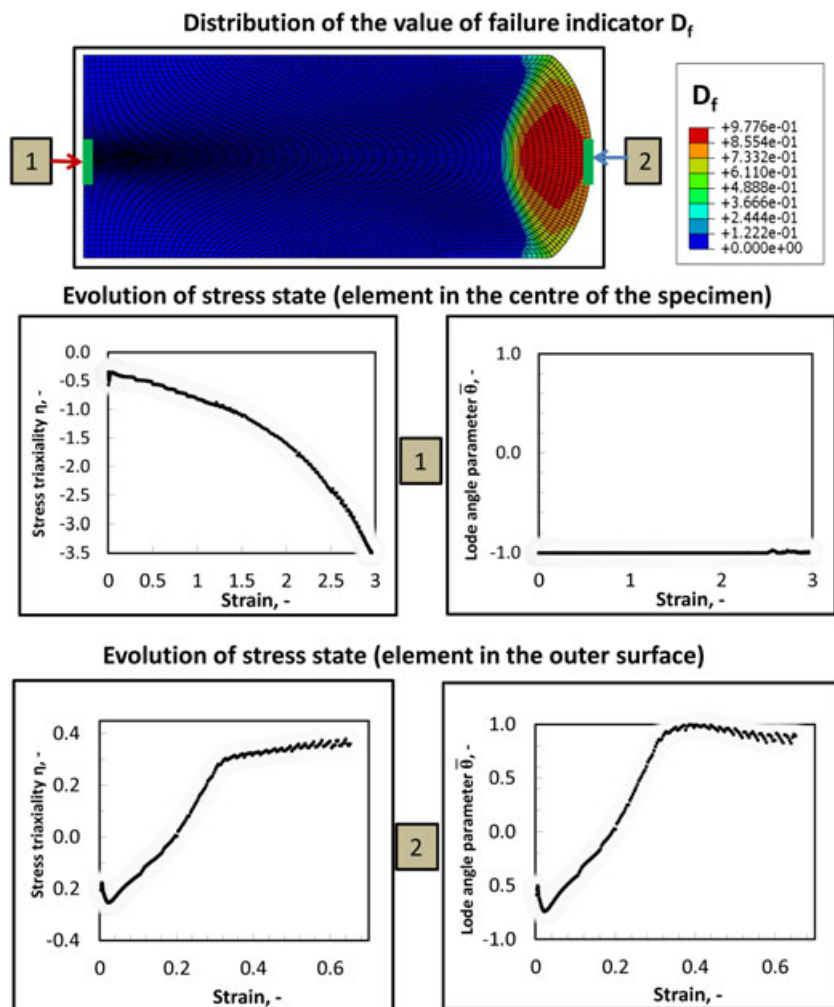


FIGURE 14 Distribution of the failure indicator D_f in the modelling of a compression test and the stress-state evolution at the outer surface and in the centre of the specimen [Colour figure can be viewed at wileyonlinelibrary.com]

uniaxial compression ($\eta = -1/3$, $\bar{\theta} = -1$) to uniaxial tension ($\eta = 1/3$, $\bar{\theta} = 1$). As stated before, this work aims to predict the damage behaviour for non-proportional strain paths under macroscopic monotonic loading conditions without consideration of kinematic hardening. Although the outer surface is already subject to a reverse loading, this simple

cycle of nonmonotonic loading in a small local region of the specimen does not significantly influence the macroscopic behaviour. Therefore, the results are still reliable.

The force-displacement curves and the time instant of macro crack formation at the surface are plotted in Figure 15A for two specimens with different H/D ratios.

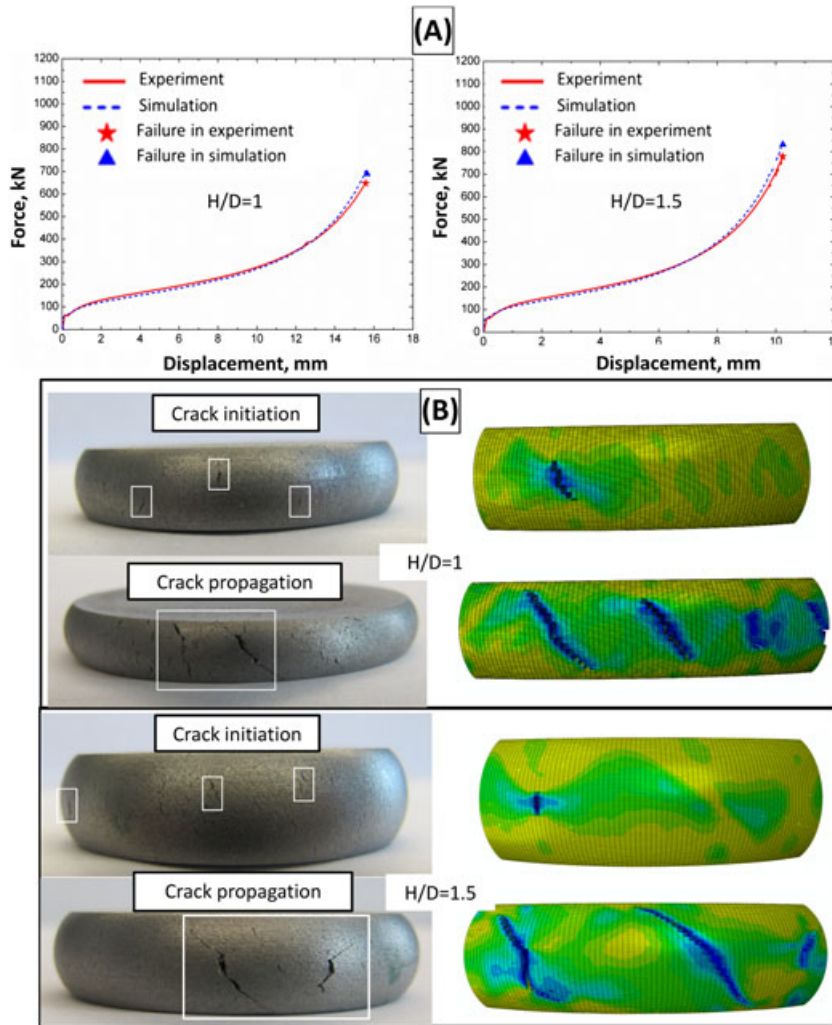


FIGURE 15 A, Comparison of force-displacement curves between the simulations and experimental results and B, comparisons of the crack morphologies at the surfaces of the specimens [Colour figure can be viewed at [wileyonlinelibrary.com](https://onlinelibrary.wiley.com/doi/10.1111/ffe.12645)]

The simulations accurately predict the forces and damage behaviour. The macro crack development was recorded in the experiments, and in the simulations, elements were removed when the failure criterion was fulfilled. The comparisons between the well-predicted and experimental crack morphologies at the surfaces of the two specimens are shown in Figure 15B. Typical shear failure with crack propagation at a 45° angle in the early stage of compression was not observed in our investigation due to the relatively high failure strain under shear, which can be seen in the previously calibrated DIL and D_{cr} locus. The cracks appeared after significant plastic deformation. The vertical macro cracks initiate at the surface of the specimen and then propagate along the shear plane.

8 | CONCLUSIONS AND OUTLOOK

In this study, an enhanced MBW model considering the influences of the stress state and strain paths was proposed and calibrated for the C45E + N steel.

The experimental results demonstrated that both damage initiation and damage propagation are dependent on the stress triaxiality and Lode angle. Therefore, a D_{cr} locus with respect to the stress triaxiality and Lode angle parameter was proposed for the enhanced model in this work. This study also demonstrated the influence of strain paths and introduced the damage initiation and failure indicators as well as weighting schemes for their evolution laws to extend the applicability of the MBW model for non-proportional loading conditions. The cut-off value integrated in the material model is important for modelling the compression tests conducted in this work, in which the inner parts of the compression specimens were severely deformed under low negative stress triaxialities. We carefully analysed the stress state and loading paths in the two-step tensile test and compression tests. The specimens are subject to complex loading paths with varying stress states in these tests. The force-displacement curves, time instant of failure, and fracture morphologies were accurately predicted using this enhanced model. The model shows high potential for applications in which complex stress state and loading histories should be considered.

Although the model has high accuracy in predictions, it has a large number of parameters, which makes the calibration and implementation more complex. In addition, the model still has some limitations. First, the applied model is implemented with local formulations. A constant mesh size of 0.15 mm was used in this study for all of the models to consider the mesh dependence. Second, the plasticity model does not consider the kinematic hardening and anisotropy. In the future, for a more generalised application of this model in cyclic loadings or for materials exhibiting plasticity anisotropy, a more advanced plasticity model that considers these aspects is required. Finally, the model was validated with the global load-deformation response. In the future, an experimental set-up with local strain measurements could help to improve the validation process.

ACKNOWLEDGEMENTS

This work was supported by the German Research Foundation (German: Deutsche Forschungsgemeinschaft) through the project “Prediction of Chip Breakage with Damage Mechanics Approaches.” (German: Vorhersage von Spanbruch bei der Zerspanung mit geometrisch bestimmter Schneider mit Hilfe schädigungsmechanischer Ansätze, BL 402/33-1, KL 500/82-1).

REFERENCES

- Bao Y, Wierzbicki T. A comparative study on various ductile crack formation criteria. *J Eng Mater Technol*. 2004;126:314-324.
- McClintock FA. A criterion of ductile fracture by the growth of holes. *J Appl Mech*. 1968;35:363-371.
- Rice JR, Tracey DM. On the ductile enlargement of voids in triaxial stress fields. *J Mech Phys Solids*. 1969;17:201-217.
- Gurson AL. Continuum theory of ductile rupture by void nucleation and growth: Part I—Yield criteria and flow rules for porous ductile media. *J Eng Mater-T ASME*. 1997;99:2-15.
- Tvergaard V, Needleman A. Analysis of the cup-cone fracture in a round tensile bar. *Acta Metall*. 1984;32:157-169.
- Nielsen KL, Tvergaard V. Ductile shear failure or plug failure of spot welds modelled by modified Gurson model. *Eng Fract Mech*. 2010;77:1031-1047.
- Nahshon L, Hutchinson J. Modification of the Gurson model for shear failure. *Eur J Mech A-Solid*. 2008;27:1-17.
- Xue L. Constitutive modeling of void shearing effect in ductile fracture of porous materials. *Eng Fract Mech*. 2008;75:3343-3366.
- Nguyen NT, Kim DY, Kim HY. A continuous damage fracture model to predict formability of sheet metal. *Fatig Fract Eng Mater Struct*. 2013;36:202-216.
- Kachanov LM. Rupture time under creep conditions. *Int J Fract*. 1999;97:11-18.
- Lemaitre J. A continuous damage mechanics model for ductile fracture. *J Eng Mater Technol*. 1985;107:83-89.
- Lemaitre J. *A Course on Damage Mechanics*. Berlin, Germany: Springer-Verlag; 1992.
- Johnson GR, Cook WH. Fracture characteristics of three metals subjected to various strains, strain rates, temperatures and pressures. *Eng Fract Mech*. 1985;21:31-48.
- Bao Y, Wierzbicki T. On the cut-off value of negative triaxiality for fracture. *Eng Fract Mech*. 2005;72:1049-1069.
- Dunand M, Mohr D. On the predictive capabilities of the shear modified Gurson and the modified Mohr-Coulomb fracture models over a wide range of stress triaxialities and Lode angles. *J Mech Phys Solids*. 2011;59:1374-1394.
- Bai Y, Wierzbicki T. A new model of metal plasticity and fracture with pressure and Lode dependence. *Int J Plasticity*. 2008;24:1071-1096.
- Besson J. Continuum models of ductile fracture: a review. *Int J Damage Mech*. 2010;19:3-52.
- Lian L, Sharaf M, Archie F, Münstermann S. A hybrid approach for modeling of plasticity and failure behavior of advanced high-strength steel sheets. *Int J Damage Mech*. 2013;22:188-218.
- Lian J, Jia XX, Münstermann S, Bleck W. A generalized damage model accounting for instability and ductile fracture for sheet metals. *Key Eng Mater*. 2014;611:106-110.
- Lian J, Wu J, Münstermann S. Evaluation of the cold formability of high-strength low-alloy steel plates with the modified Bai-Wierzbicki damage model. *Int J Damage Mech*. 2015;24:383-417.
- Buchkremer S, Wu B, Lung D, Münstermann S, Klocke F, Bleck W. FE-simulation of machining processes with a new material model. *J Mater Process Technol*. 2014;214:599-611.
- Basu S, Benzerga AA. On the path-dependence of the fracture locus in ductile materials: Experiments. *Int J Solids Struct*. 2015;71:79-90.
- Benzerga AA, Surovik D, Keralavarma SM. On the path-dependence of the fracture locus in ductile materials analysis. *Int J Plasticity*. 2012;37:157-170.
- Bao Y, Roland T. Ductile crack formation on notched Al2024-T351 bars under compression-tension loading. *Mater. Sci. Eng. A-struct*. 2004;384:385-394.
- Derpinski L, Seweryn A. Ductile fracture of EN-AW 2024 aluminum alloy specimens with notches under biaxial loading. Part 2—numerical research and ductile fracture criterion. *Theor Appl Fract Mec*. 2016;84:203-214.
- Berto L, Cendón DA, Elices M. Fracture behavior under torsion of notched round bars made of gray cast iron. *Theor Appl Fract Mec*. 2016;84:157-165.
- Marcadet SJ, Mohr D. Critical hardening rate model for predicting path-dependent ductile fracture. *Int J Fract*. 2016;200:77-98.
- Marcadet SJ, Mohr D. Effect of compression-tension loading reversal on the strain to fracture of dual phase steel sheets. *Int J Plasticity*. 2015;72:21-43.
- Hariharan K, Barlat F, Lee MG, Prakash RV. Extension of strain-life equation for low-cycle fatigue of sheet metals using anisotropic yield criteria and distortional hardening model. *Fatig Fract Eng Mater Struct*. 2014;37:977-991.
- Lemaitre J. Coupled elasto-plasticity and damage constitutive equations. *Comput Methods Appl Mech Eng*. 1985;51:31-49.

31. Lemaitre J, Desmorat R. *Engineering Damage Mechanics*, Berlin/Heidelberg, Germany: Springer-Verlag; 2005.
32. Hosford WF. A generalized isotropic yield criterion. *J Appl Mech*. 1972;39:607-609.
33. Karafillis AP, Boyce MC. A general anisotropic yield criterion using bounds and a transformation weighting tensor. *J Mech Phys Solids*. 1993;41:1859-1886.
34. Teng X, Wierzbicki T. Evaluation of six fracture models in high velocity perforation. *Eng Fract Mech*. 2006;73:1653-1678.
35. Lou Y, Huh H, Lim S, Pack K. New ductile fracture criterion for prediction of fracture forming limit diagrams of sheet metals. *Int J Solids Struct*. 2012;49:3605-3615.
36. Wu B, Buchkremer S, Münstermann S, et al. Modeling of Chip Breakage in Machining of AISI 1045 Steel by Using an Improved Damage Mechanics Model. *Steel Res Int*. 2017. <https://doi.org/10.1002/srin.201600338>
37. Silva CMA, Alves LM, Nielsen CV, Atkins AG, Martins PAF. Failure by fracture in bulk metal forming. *J Mater Process. Tech*. 2015;215:287-298.
38. Di Y, Lian J, Wu B, et al. The second blind sandia fracture challenge: improved MBW model predictions for different strain rates. *Int J Fract*. 2016;198:149-165.
39. Novoksharov D, Döbereiner B, Sharaf M, Münstermann S, Lian J. A new model for upper shelf impact toughness assessment with a computationally efficient parameter identification algorithm. *Eng Fract Mech*. 2015;148:281-303.

How to cite this article: Wu B, Li X, Di Y, Brinell V, Lian J, Münstermann S. Extension of the modified Bai-Wierzbicki model for predicting ductile fracture under complex loading conditions. *Fatigue Fract Eng Mater Struct*. 2017;40:2152–2168. <https://doi.org/10.1111/ffe.12645>